Tuning the Laser-Induced Processing of 3D Porous Graphenic Nanostructures by Boron-Doped Diamond Particles for Flexible Microsupercapacitors

Sujit Deshmukh,* Pawel Jakobczyk, Mateusz Ficek, Jacek Ryl, Dongsheng Geng, and Robert Bogdanowicz*

Carbon (sp³)-on-carbon (sp²) materials have the potential to revolutionize fields such as energy storage and microelectronics. However, the rational engineering and printing of carbon-on-carbon materials on flexible substrates remains a challenge in wearable electronics technology. This study demonstrates the scalable fabrication of flexible laser-induced graphene (LIG)-boron doped diamond nanowall (BDNW) hybrid nanostructures for microsupercapacitors. Direct laser writing on polyimide film is tuned by the presence of BDNW powder where an appreciable absorbance of the BDNWs at the CO_2 laser wavelength enhances the local film temperature. The thermal shock due to laser irradiation produces graphitized and amorphous carbon at the diamond grain boundaries which increases the thermal and charge transfer capacity between the LIG–diamond interfaces. The samples are further treated with O_2 plasma to tune the wettability or to improve the microsupercapacitor device performance. The outstanding electrical characteristics of graphene, exceptional electrochemical stability of diamond, and essential contributions of oxygen-containing groups result in a remarkable charge storage capacity (18 mF cm^{-2} @ 10 mV s^{-1}) and cyclic stability (98% retention after 10 000 cycles) outperforming most state-of-the-art LIG-based supercapacitors. Furthermore, despite extreme mechanical stress, these microsupercapacitors maintain their outstanding electrochemical properties, thus holding promise for high-power, flexible/wearable electronics.

1. Introduction

The current trend in portable electronic devices is to continue miniaturization while improving the functionality and durability of existing device components. However, the integration of the two main energy storage units (batteries and supercapacitors) with miniaturized electronic circuits is often challenging for flat and rigid devices.[1] Due to this, the demand for flexible and portable electronic devices has become increasingly urgent.[2–4] In line with this, the progress in miniaturized micro-device technology has made it possible to construct interdigitated flexible microsupercapacitors (MSCs) which substitute the conventional sandwich structure which is incompatible with integrated circuits.[5,6] These in-plane flexible MSCs feature high power density, a fast charge/discharge rate, and long-term cycling stability. As a result, MSCs complement or even sometimes replace micro batteries in wearable electronics where high power delivery and long life cycles are required.

Recently, a graphene-based material known as laser-induced graphene (LIG) has been synthesized at a large scale on flexible polymer surfaces using a low-cost laser printing technology, making them potentially cost-effective materials for charge storage devices.[7,8] Direct laser writing of LIG can create any desired interdigitated pattern with nanoscale dimensions, making it more versatile for MSCs than other carbon-based materials such as carbon nanotubes,[9,10] carbide-derived carbons,[11,12] and so on.[13] However, while the pioneering idea

S. Deshmukh, P. Jakobczyk, M. Ficek, R. Bogdanowicz
Department of Metrology and Optoelectronics
Faculty of Electronics
Telecommunications and Informatics
Gdansk University of Technology
11/12 G. Narutowicza Str, Gdansk 80-233, Poland
E-mail: sujit.deshmukh@pg.edu.pl; rbogdan@eti.pg.edu.pl

The ORCID identification number(s) for the author(s) of this article can be found under https://doi.org/10.1002/adfm.202206097.

J. Ryl
Institute of Nanotechnology and Materials Engineering
Gdansk University of Technology
11/12 Narutowicza Str, Gdansk 80-233, Poland

D. Geng
Beijing Advanced Innovation Center for Materials Genome Engineering
Beijing Key Laboratory for Magneto-Photoelectrical Composite
and Interface Science
School of Mathematics and Physics
University of Science and Technology Beijing
Beijing 100083, P. R. China

of laser scribing developed by Kaner et al. to prepare flexible MSCs has shown outstanding power performance, but was unable to attain high areal capacitance (<5 mF cm^{-2}).[1,6] Later on, Tour et al. demonstrated a single-step lasing process to pattern interdigitated electrodes on commercial polyimide (PI) sheets, but it also fails to achieve high areal capacitance.[8] Another strategy applied afterward is to combine pseudocapacitive materials (such as MnO_2, TiO_2, VO_x, etc.) with LIG to extract a higher capacitance value, but moving from a pure electrical double layer to a pseudocapacitive component has a number of drawbacks, including reduced power capability and long cycling stability due to the kinetic limitation of the redox reaction.[14–18] By integrating another stable material into the 3D network of LIG, we may improve its conductivity and ion diffusion length, resulting in a GOOD capacitor electrode. Since the energy density of MSC devices is determined by their specific capacitance and working potential window ($E = \frac{1}{2}\,CV^2$), improving any of these parameters will further improve energy storage performance.[19] Therefore, to construct a good MSC device using LIG, we need to combine it with another stable material that ensures high capacitance, wide potential window, improved conductivity, and a long life cycle.

As a supercapacitor electrode, sp^3 forms of carbon, such as nanostructured conductive nanocrystalline diamond (boron-doped diamond), have recently been used with great success.[20] Integrating boron-doped diamond (BDD) with the 3D network of LIG is advantageous for the following reasons. BDDs are electrochemically stable in their operating potential window, highly electroactive, electrically conductive, and have high tensile strength which is beneficial for improving the energy and power density of diamond-based supercapacitor devices.[21–23] Moreover BDDs are chemically inert and stable in a wide range of corrosive electrolytes such as fluoride, alkaline, and mixtures of strong acids (H_2SO_4, HNO_3, etc.).[24–27] Electrochemically, BDD can be used from −35 to +6 V without suffering any damage to its surface.[28] This wide potential window and electrochemical (EC) stability bring diamonds to the forefront to be applied as high-energy-density devices.[23,29,30] However most of the carbon-based SCs the electrode materials are mixed with organic binders before being pressed or coated on the current collector.[31] As a result, both ion mobility inside the capacitor and ion diffusion on the capacitor's surfaces are hindered by the organic binder's low conductivity and poor stability. Binder-free capacitor electrode is therefore highly needed to construct a better SC device.

The binder-free carbon capacitor electrodes based on a hybrid structure of BDD and LIG will offer the dual advantages of both sp^3 and sp^2 carbon and may resolve the key bottlenecks for the construction of MSC devices using LIG alone. The excellent charge transfer between the LIG and BDD through the combination of sp^3 and sp^2 C−C bonds can make the LIG-BDD hybrid a promising electrode material for energy storage devices. Furthermore, using considerably low photon energy as compared to the bandgap of diamonds (≈5.5 eV), CO_2 laser irradiation can photothermally degrade the diamond grain boundaries by converting nanodiamonds into graphitized and/or amorphous carbon, which improves the charge transfer kinetics at the LIG-BDD interfaces.[32,33] However, previously published LIG-based MSCs had poor EC performance because macropore-dominated porous 3D graphene is hydrophobic in

nature.[34,35] Therefore, in addition to make a BDD/LIG hybrid, it is necessary to improve the wettability of the LIG for high-performance MSCs.

In consideration of the aforementioned issues described above, we report here the direct fabrication of in-plane inter-digitated LIG-boron-doped diamond nanowall (BDNW) hybrid on a flexible substrate (PI sheet). We treated the LIG-BDNW hybrid with a room-temperature oxygen plasma to tune the underlying surface wettability, which allowed better contact between the hybrid structures and the electrolyte. Proposed process is readily scalable and devices are prepared on large scale maintaining their flexibility. The as-fabricated electrodes are used as symmetric double-layer MSCs using both polymer gel (PVA/H_2SO_4) and ionogel electrolyte (EMIMBF$_4$/PAN/TMS) and thanks to the intrinsic mechanical flexibility of PI sheet, the MSC devices are shown to possess exceptional EC stability and retention under different bending conditions. All the designed devices revealed energy densities comparable to microbatteries while maintaining excellent rate performance, cycle stability, and mechanical flexibility.
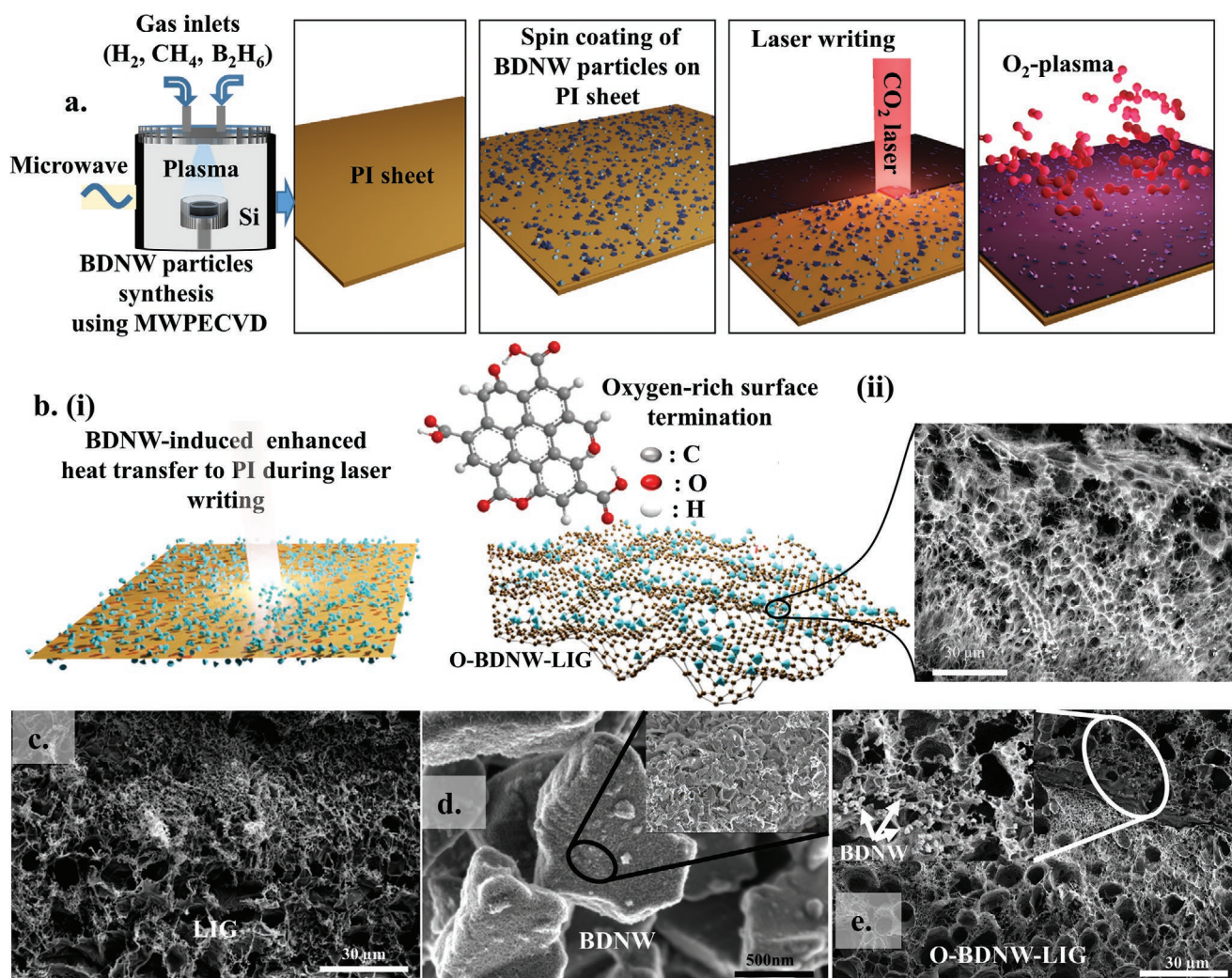
2. Results and Discussion

A schematic diagram for the fabrication of diamond-LIG hybrid MSC devices is shown in **Figure 1**a. First, the BDNW particles are synthesized using a MWPECVD system (details are included in the Experimental Section). The supporting information file contains a brief Techno-Economic discussion of the fabrication cost of BDD. Next, the flexible PI sheet was coated with BDNW particles by the spin-coating method. Afterward, a CO_2 laser (10.6 µm) was used for direct writing on the BDNW-coated PI sheet to prepare the BDNW-LIG hybrid. When the BDNW-modified PI surface was irradiated with a laser, in situ decoration of the BDNW particles inside the 3D porous network of LIG was achieved. Before adding solid-state electrolyte on the BDNW-LIG hybrid the sample was treated with low-temperature O_2 plasma.

When the PI sheet was irradiated with a CO_2 laser, the local temperature of the laser interaction zone climbed up to 2000 °C causing carbonized steam to form and some gases (O_2, CO, CO_2, CH_4, N_2, etc.) to be released at a temperature exceeding 700 °C.[8,36,37] The rapid release of gaseous products resulted in a 3D porous interconnected structure of the LIG (Figure 1c).

Figure 1d shows a scanning electron microscopy (SEM) image of the BDNW particles, where well-faceted diamond particles (particles size ≈ 1–2 µm) with distinguishable edges can be seen. A high-magnification SEM image (inset of Figure 1d) confirms the dense and curled nanowall type morphology of the diamond particles. These nanowalls are arranged randomly with the lengths of the nanowalls observed to vary in the range of 100–500 nm.

As depicted in Figure 1e, O-BDNW-LIG was prepared by laser scribing on the BDNW-coated PI film followed by O_2 plasma treatment, which is known to create rougher edges, surface defects, and oxygen-containing groups on carbon materials.[38,39] Even though diamond has a wide bandgap of ≈5.5 eV, the instantaneous high-temperature thermal shock degrades the BDNWs and strong optical absorption takes place.[40,41] This optical absorption in the IR range further increased the local film temperature of the PI sheet which facilitates the release of gaseous products resulting in the formation of a BDNW-decorated LIG

**ADVANCED
SCIENCE NEWS**

www.advancedsciencenews.com

**ADVANCED
FUNCTIONAL
MATERIALS**

www.afm-journal.de

Figure 1. a) Schematic diagram showing the fabrication of diamond-LIG hybrid. b) (i) Schematic illustration demonstrating appreciable IR absorption of the BDNW particles raises PI film temperature resulting in a wrinkled shape LIG surface coated with BDNW particles. The schematic diagram of the oxygen-rich surface termination is also displayed. (ii) SEM top-view of the BDNW-LIG surface, where diamond particles (white spots) are uniformly distributed across the LIG. c) SEM image LIG film showing a porous morphology. d) SEM image BDNW particles with magnified image in inset showing a randomly oriented nanowall-like morphology. e) SEM image of O-BDNW-LIG with a magnified image in inset showing the BDNW particles decoration over the LIG network.

surface (Figure 1b). The O_2 plasma treatment creates discrete pores with a diameter ranging from 5 to 10 μm throughout the LIG surface. The SEM image indicates the formation of microvoids due to the O_2 plasma treatment which increases the surface roughness and large volume of trapped air in these microvoids. These trapped air are responsible for increasing the sheet resistance of the O-BDNW-LIG (discussed later). Although this type of surface roughness is beneficial for improving hydrophobicity, the O_2 plasma treatment oxidizes the graphene edges (Figure 1b), making them hydrophilic and water droplets quickly sink inside this porous O-BDNW-LIG structure (Movie S1, Supporting Information). The successful decoration of BDNW particles on the LIG surface can also be seen in Figure 1e. A high-magnification SEM image (Figure 1b and inset of Figure 1e) makes the micron-sized BDNW particles more apparent, implying that BDNWs are uniformly distributed across the LIG surface. Figure S2 (Supporting Information) shows the cross-sectional SEM images of all the samples, revealing that

the O-BDNW-LIG has a maximum thickness of approximately 84 μm. The morphology of the O-LIG (Figure S3, Supporting Information) is similar to that of the O-BDNW-LIG. The diamond incorporation and O_2 plasma treatment have a significant impact on the LIG MSC device performance. The degree/type of defects induced in the LIG surface due to oxygenation and diamond incorporation is analyzed further by X-ray diffraction (XRD) and Raman spectroscopy studies.

XRD measurements were performed to differentiate the various carbonaceous phases present in the LIG and LIG-BDNW composites, and the results are shown in **Figure 2**a. Two well-distinguished peaks were observed for the samples BDNW at $2\theta = 43.7°$ and $75.2°$, corresponding to the (111) and (220) planes of polycrystalline diamond, respectively.[42] The XRD pattern of LIG consists of an intense peak cantered around $2\theta \approx 26°$ corresponding to the (002) plane of graphite with an interlayer spacing of 3.4 Å which indicates a high degree of graphitization. Interestingly, for the composite samples (BDNW-LIG and

**ADVANCED
SCIENCE NEWS**
www.advancedsciencenews.com

**ADVANCED
FUNCTIONAL
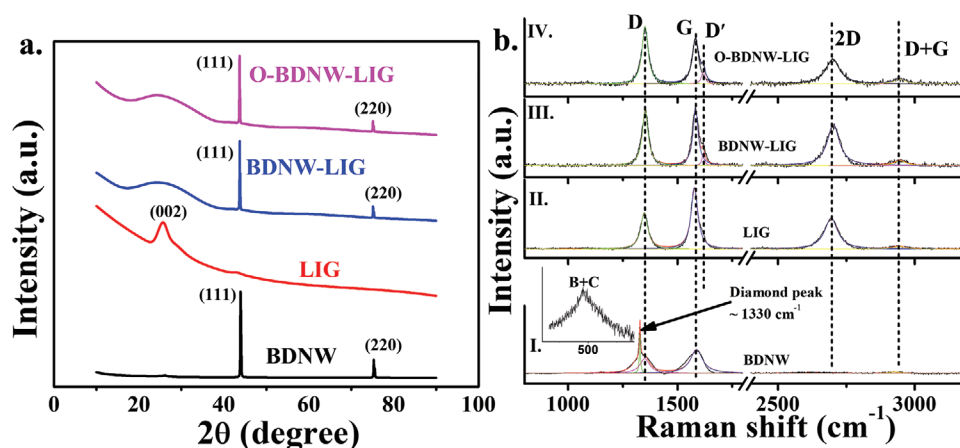MATERIALS**
www.afm-journal.de

Figure 2. a) XRD and b) Raman spectra of BDNW, LIG, BDNW-LIG, and O-BDNW-LIG films.

O-BDNW-LIG), a broad diffraction peak around $2\theta \approx 25°$ was witnessed along with polycrystalline diamonds (111) and (220) peaks. The broad diffraction peak in the composite samples can be assigned as disordered graphite which is similar to the previous findings of reduced graphene oxide.[43] The XRD results confirm the formation of diamond/graphene composite with a single-step laser process. However, the degree of graphitization is less for the BDNW-LIG and O-BDNW-LIG composites as compared to LIG. The lower degree of graphitization was caused by the access heat dissipation during the laser irradiation due to the presence of BDNW particles on the PI surface.

Raman spectroscopy was used to determine the types of defects and growing disorders in the LIG network as a result of diamond nanowall incorporation and oxygen plasma treatment. The Raman spectrum of BDNW powder [Figure 2b (I)] shows a sharp diamond peak around 1328 cm^{-1} and the peak sharpness (full width at half maximum $\approx$ 7 cm^{-1}) indicates the high crystallinity of the sp^3-hybridized carbons.[44] The magnified view of the region from 100 to 800 cm^{-1} is shown in the inset of Figure 2b (I) and the full spectrum is shown in Figure S4 (Supporting Information). The occurrence of boron in the BDNW particles is confirmed by a prominent peak at around 455 cm^{-1}.[45] The presence of weak bands around 1586 cm^{-1} (G band) and 1350 cm^{-1} (D band) is attributed to traces of sp^2 carbon and disorder in the sp^2 carbon, respectively.[46] In the case of LIG [Figure 2b (II)], the Raman spectrum has three primary peaks: the D peak $\approx$1350 cm^{-1}, the G peak $\approx$1580 cm^{-1}, and the 2D peak $\approx$2700 cm^{-1} originating from second-order zone-boundary phonons.[8] The 2D band of the LIG is fitted with a single Lorentzian peak centered around 2700 cm^{-1} with a full width at half maximum of 55 cm^{-1}. This kind of 2D profile is typical as observed in the few layers of graphene stacked along the C axis.[35,47] The Raman signal of the BDNW-LIG [Figure 2b (III)] and O-BDNW-LIG [Figure 2b (IV)] displays the same main features (D, G, and 2D band) as observed in the LIG. However, when comparing the spectra of the BDNW-LIG to the spectra of the LIG, we noticed three significant alterations: 2D band blueshift of $\approx$7 cm^{-1}, D band intensity is increased, and a asymmetric G peak or the appearance of a D' peak around 1615 cm^{-1}. The bond angle disorder and compressive stress at the LIG/diamond/nanowall interfaces cause the 2D band blueshift.[48] The intense D peak and the presence of the D'

peak are related to defects in the BDNW-LIG substrate, and the intensity of the D and D' are proportional to the concentration of defects n_d.[49] By fitting the data, we obtained the high relative intensity of the D and D' peaks, $I_{D/D'}$, of $\approx$13 for BDNW-LIG, suggesting the D peak rises mainly from the sp^3 defects rather than vacancies or grain boundary defects.[50] The D band intensity is further increased for the O-BDNW-LIG sample. The $I_{D/G}$ ratio increases so as the FWHM of the D band, indicating the oxygen functional groups have a strong impact on the in-plane sp^2 domains of the O-BDNW-LIG with defects. The peaks correspond to the overtones (2D and D+G) also display significant changes due to the oxidation process. The 2D band intensity decreases, and so does the $I_{2D/G}$ ratio, which indicates a decline in crystallinity as a result of oxidation.[51] Interestingly, the $I_{D/D'}$ ratio of the O-BDNW-LIG is decreased to 7 when compared to the BDNW-LIG, indicating defects associated with vacancies.[50] The extracted fitted parameter from the Raman analysis is listed in Table S1 (Supporting Information). The Raman analysis, therefore, provides a clear image of the sorts of defects induced on the sp^2 network of the LIG as a result of diamond/nanowall inclusion and oxidation processes.

A high-resolution transmission electron microscopy (HRTEM) study further confirms the presence of diamond lattice in the BDNW powder and the few-layer characteristics of the LIG. Diamond lattice planes {111} are identifiable in a typical HRTEM image (**Figure 3**a,b) of the BDNW particle. The distance between two successive fringes is about 0.20 nm which agrees well with diamond {111} planes of nanodiamond crystal.[52] The formation of amorphous carbon and graphitized layers is evidenced along the grain boundaries of the diamond crystallites. Internal graphitization at the grain boundary degrades the optical quality of the diamond particles, resulting in a significant increase in IR absorption (10.6 μm) during CO_2 laser irradiation.[40] On the other hand, a typical HRTEM image of the LIG in Figure 3c reveals that the interlayer spacing is $\approx$0.35 nm which corresponds to the (002) plane of graphite. The signature of the few-layer graphene structure and the characteristic wrinkles of the graphitized PI film caused due to compressive strain during laser irradiation are visible on the LIG surface.[8,35]

The atomic ratio of carbon to oxygen (C/O) is quantitatively characterized from the X-ray photoelectron spectroscopy (XPS) survey scan graph (Figure S5, Supporting Information) and the
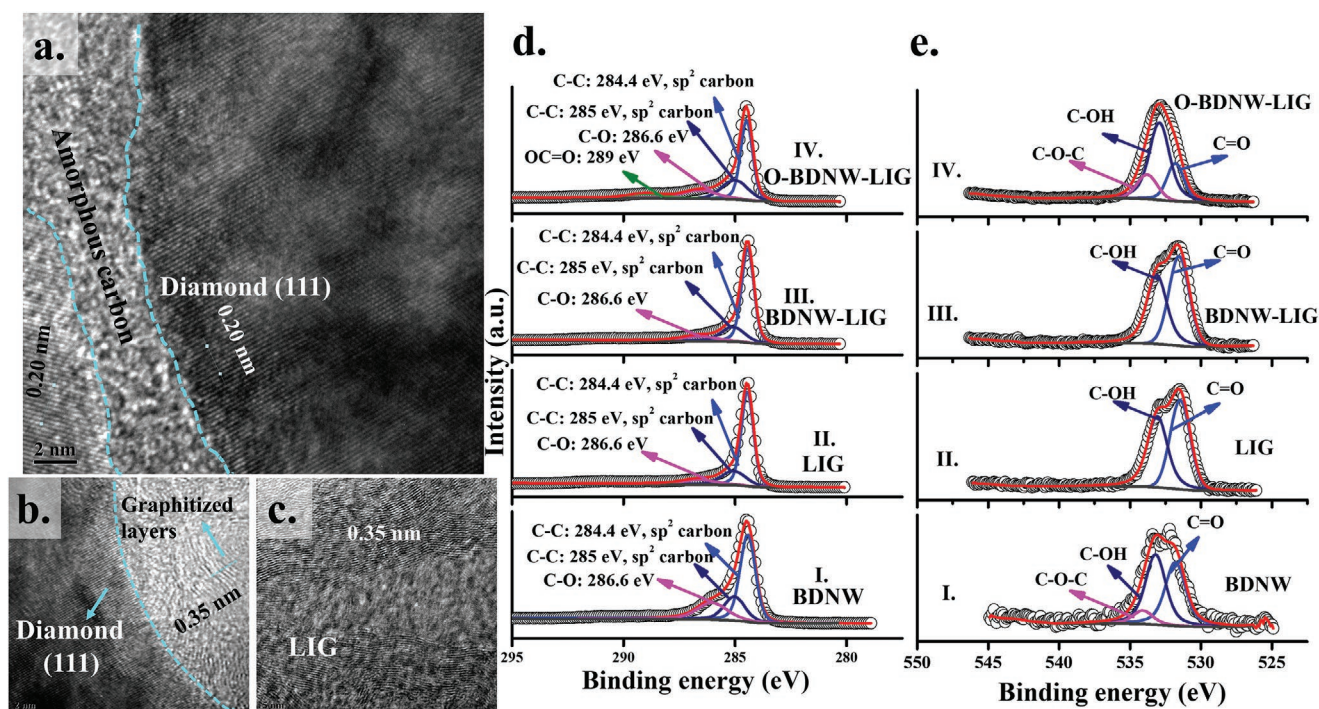
Figure 3. a,b) HRTEM images of BDNW particles showing diamond (111) planes surrounded by amorphous carbon and graphitized carbon, respectively. Scale bar 2 nm. c) HRTEM image of LIG, lattice spacing of around 0.35 nm corresponds to the (002) planes of graphitized materials. Scale bar 5 nm. d) High-resolution C1s XPS spectra and e) High-resolution O1s XPS spectra of (I) BDNW, (II) LIG, (III) BDNW-LIG, and (IV) O-BDNW-LIG films.

results are summarized in Table S2 (Supporting Information). The oxygen plasma treatment had a significant influence on the O-BDNW-LIG when compared to the bare BDNW, LIG, and BDNW-LIG, as the amount of oxygen atoms in the O-BDNW-LIG significantly increased. The BDNW, LIG, and BDNW-LIG had C/O values of 33.8 12.8, and 10.8, respectively, whereas the value was considerably reduced to 6.1 for the O-BDNW-LIG sample. This implies that a large number of oxygen-containing groups were introduced randomly on the planer sp^2 hybridized benzene rings: in other words, the sp^2 hybridized benzene rings were separated by the sp^3 carbons, which lead to a higher sheet resistance of the O-BDNW-LIG as compared to the other samples.[35,53] The deconvolution of the high-resolution C 1s and O 1s XPS spectra (Figure 3d,e) clarifies this further. The primary constituents of the BDNW sample were sp^2 carbon (≈53 at%) and sp^3 carbon (≈30 at%) located around 284.5 and 285.1 eV, respectively [Figure 3d(I)]. Notably, the sp^2 to sp^3 ratio calculated based on the deconvolution is ≈1.8, which is consistent with previously published results.[54] This aforementioned sp^2 carbon-dominated BDNW structure originated from the substitutional boron on the diamond lattice.[55] However, the boron percentage (B/C ≈ 2000 ppm) was too low to be detected in the XPS spectra. The XPS C 1s spectra of all LIG-based thin film samples were dominated by the C—C contribution (284.5 ± 0.1 eV) implying that the LIG films were mainly dominated by sp^2 carbons, which is consistent with the Raman observations. Other carbon components such as sp^3 hybridized carbon (285.1 ± 0.1 eV) and residual C—O components (286.4 ± 0.1 eV) were also found in all of the samples. However, an extra contribution from the OC=O peak of the

O-BDNW-LIG at around 289.0 eV which is absent for the other samples plays an important role in modulating the wettability and improving the MSC device performance. The extracted binding energy and corresponding contribution of the carbon bonds are charted in Table S2 (Supporting Information). The sp^2 carbon content is highest on the LIG surface, whereas the BDNW has the highest fraction of sp^3 carbon.

To detect the evolution of the oxygenated groups, the O 1s XPS core level spectra are further deconvoluted. As shown in Figure 3e, the high-resolution O 1s spectrum of each sample can be divided into two types of oxygenated groups: C=O (531.7 ± 0.2 eV) and C—OH (532.6 ± 0.2 eV) with an exception for O-BDNW-LIG where an extra peak corresponding to the C—O—C groups (≈533.8 eV) is spotted.[56–58] These epoxy groups (C—O—C) are quickly converted into hydroxyl groups (C—OH) in the presence of acidic media via the ring-opening reaction.[59] Therefore, the peak centered around 533.8 eV can be classified as C—OH as well.

The presence of oxygenated groups has a significant influence on modulating the underlying wettability and sheet resistance of the LIG–diamond hybrid, which are discussed next.

Figure S6 (Supporting Information) shows the water contact angle values of the LIG and BDNW-LIG samples. The as-prepared LIG surface made in the ambient atmosphere is hydrophobic in nature (LIG_{WCA} ≈ 120°) and it becomes hydrophilic when the LIG is decorated with the BDNW particles ($BDNW-LIG_{WCA}$ ≈ 70°), while the BDNW-LIG sample exposed to O_2 plasma show superhydrophilicity ($O-BDNW-LIG_{WCA}$ ≈ 0°, Movie S1, Supporting Information). From the XPS analysis, it is confirmed that the LIG samples had a lower oxygen content

**ADVANCED
SCIENCE NEWS**

www.advancedsciencenews.com

**ADVANCED
FUNCTIONAL
MATERIALS**

www.afm-journal.de

and oxygenated functional groups (C—O), resulting in a higher WCA. The reduction in contact angle for the BDNW-LIG can be explained based on the surface chemical state. It is well known that the surface energy of diamond (110) and (111) planes is higher (9207 and 3387 mJ m^{-2}, respectively) as compared to highly ordered pyrolytic graphite (1139 mJ m^{-2}).[60,61] This suggests the sp^3-rich surface was responsible for the enhancement of the surface energy, thereby decreasing the WCA of the BDNW-LIG film. Next, in the case of the O-BDNW-LIG, the surface chemistry changed a lot due to the O_2 plasma treatment and we can correlate the superhydrophilic nature of the O-BDNW-LIG with the oxygen content. The correlation between the WCA and oxygen content can be rationalized by the well-known fact that C—O and C=O bonds are more polar as compared to C—C and C—H.[35] The higher level of oxygen functional group means water interaction at the graphene edges are more favorable and the porous structure permits water droplets to sink into the O-BDNW-LIG structure. The increased proportion of hydroxyl group on the O-BDNW-LIG surface, which improves its hydrophilicity and facilitates better contact with the electrolyte, is one of the reasons for the better MSC device performance as compared to the other samples.

The BDNW particles result in the resistivity of ≈ 1 Ω cm as studied by a two-point probe. We have previously reported that flat BDNW structures reveal the resistivity of 4.7×10^{-4} Ω cm.[62] The boron doping impact on the conductivity of the surface was observed by electrochemical impedance spectroscopy. The flatband potential of BDNW was located in the close vicinity of the valence band, thus, the whole band offset, namely, the location of the conduction and valence bands, was modified upon boron doping.

The chemical functionality, porosity, and microstructure of the LIG/diamond hybrid have a major impact in controlling the sheet resistance (Figure S7, Supporting Information). The decoration of highly conductive BDNW into LIG's porous 3D network made the BDNW-LIG (16.73 Ω square^{-1}) less resistant than the LIG (17.81 Ω square^{-1}). Compared to the LIG and BDNW-LIG, O-LIG possessed low graphitic carbon and a more porous structure, resulting in higher sheet resistance (22.87 Ω square^{-1}). When the BDNW-LIG was treated with oxygen plasma for 5 min, a significant increase in sheet resistance was observed for the O-BDNW-LIG (30.22 Ω square^{-1}). The lowest sp^2/sp^3 ratio and the formation of a more porous structure made the O-BDNW-LIG sheet's resistance high.

Therefore, we can conclude that despite the large bandgap of sp^3 carbon (5.5 eV), an appreciable portion of the photon energy of the CO_2 (10.6 µm) laser is absorbed by the BDNW powder due to the large number of surface defects (graphitized carbon) and the amorphous carbon shell at the grain boundary.[40,41] The surface defects of the BDNW will increase further with the laser irradiances and it can significantly raise the local film temperature of the LIG surface by the photothermal process. The compressive strain is therefore increased considerably at the LIG–diamond interface causing structural disorder (wrinkles) on the LIG surface. The enhanced defects at the LIG–diamond interface due to the thermal shock from the CO_2 laser induces Shockley-type electronic states, which enhances the optical absorption.[63] We also found that the current-carrying capacity of the LIG-diamond hybrid is also improved (see Figure S7,

Supporting Information), which is attributed to the decrease in thermal resistance of the BDNW particles due to the laser irradiation.[64] The defect-induced LIG-diamond interface with Shockley-type electronic states plays an important role in the EC device performances, which are discussed next.

The EC performance of all MSC devices is evaluated in 1 V with a hydrogel polymer electrolyte [poly(vinyl alcohol) (PVA)-H_2SO_4] by cyclic voltammetry (CV) measurement at a scan rate of 10 mV s^{-1} (**Figure 4**a). All devices have a quasi-rectangular CV profile, indicating the characteristics of strong electrical double layer (EDL) capacitance. Among the three CV profiles of the MSCs, O-BDNW-LIG had the largest loop area, which highlights its superiority over the LIG and BDNW-LIG in terms of the areal capacitance (C_A) value. Before proceeding with the comprehensive electrochemical experiments, the amount of BDNW loaded is also optimized (Figure S8, Supporting Information). The CV performance is optimum with a BDNW concentration of 5 mg mL^{-1} in dimethyl sulfoxide. It can be observed that the CV curves of the O-BDNW-LIG exhibit typical capacitive features with the rectangular shape at a low scan rate of 1–20 mV s^{-1} (Figure 4b), and the high scan rate CV profiles are displayed in Figure S6 (Supporting Information). Figure 4c displays the C_A and volumetric capacitance (C_v) of the O-BDNW-LIG as a function of scan rate. Notably, the O-BDNW-LIG MSC device delivered exceptional $C_A \approx 20$ mF cm^{-2} and $C_v \approx 2.3$ F cm^{-3} at 5 mV s^{-1}, both of which are higher than the most reported LIG-based MSCs without an additional metal current collector (**Table 1**). The MSC device performance enhancement of the O-BDNW-LIG as compared to the LIG and BDNW-LIG is also proved by the longest discharge time from the triangular galvanostatic charge–discharge (GCD) profiles at the current density of 0.1 mA cm^{-2} (Figure 4d). The discharge profile consists of two sections, an abrupt potential drop (iR drop of ≈ 0.08 V) followed by the potential decay. The sudden iR drop results from the internal resistance and the succeeding potential decay represent the capacitive characteristics of the electrode. The excellent EC capacitance performance is further supported by the triangular shape of GCD curves at different current densities (Figure 4e). The capacitance of the symmetric MSC device made of O-BDNW-LIG was calculated based on the charge–discharge curves. The C_A and C_V of the O-BDNW-LIG (full device capacitance) were 7.77 mF cm^{-2} and 0.89 F cm^{-3}, respectively, at a current density of 0.2 mA cm^{-2} (Figure 4f). The C_A values are comparable to or even higher than previously developed LIG-based MSCs (Table 1).

Meanwhile, the electrochemical impedance spectra (EIS) again revealed that the O-BDNW-LIG had superior capacitive behavior compared to the LIG and BDNW-LIG, in which the O-BDNW-LIG displayed a larger slope compared with other devices in the low-frequency region (Figure S10, Supporting Information). It can be observed that in the low-frequency zone, the Nyquist plot of the O-BDNW-LIG was closest and almost parallel to the Y-axis, implying the best capacitive output. In the high-frequency region, the O-BDNW-LIG had the smallest equivalent series resistance (ESR) of ≈ 250 Ω, while the ESR values for other devices were larger than 350 Ω.[65]

The O-BDNW-LIG MSC device also showed excellent cyclic stability (Figure 4g), maintaining 98% of its initial capacitance even after the 10 000 charge/discharge cycle. To test the applicability
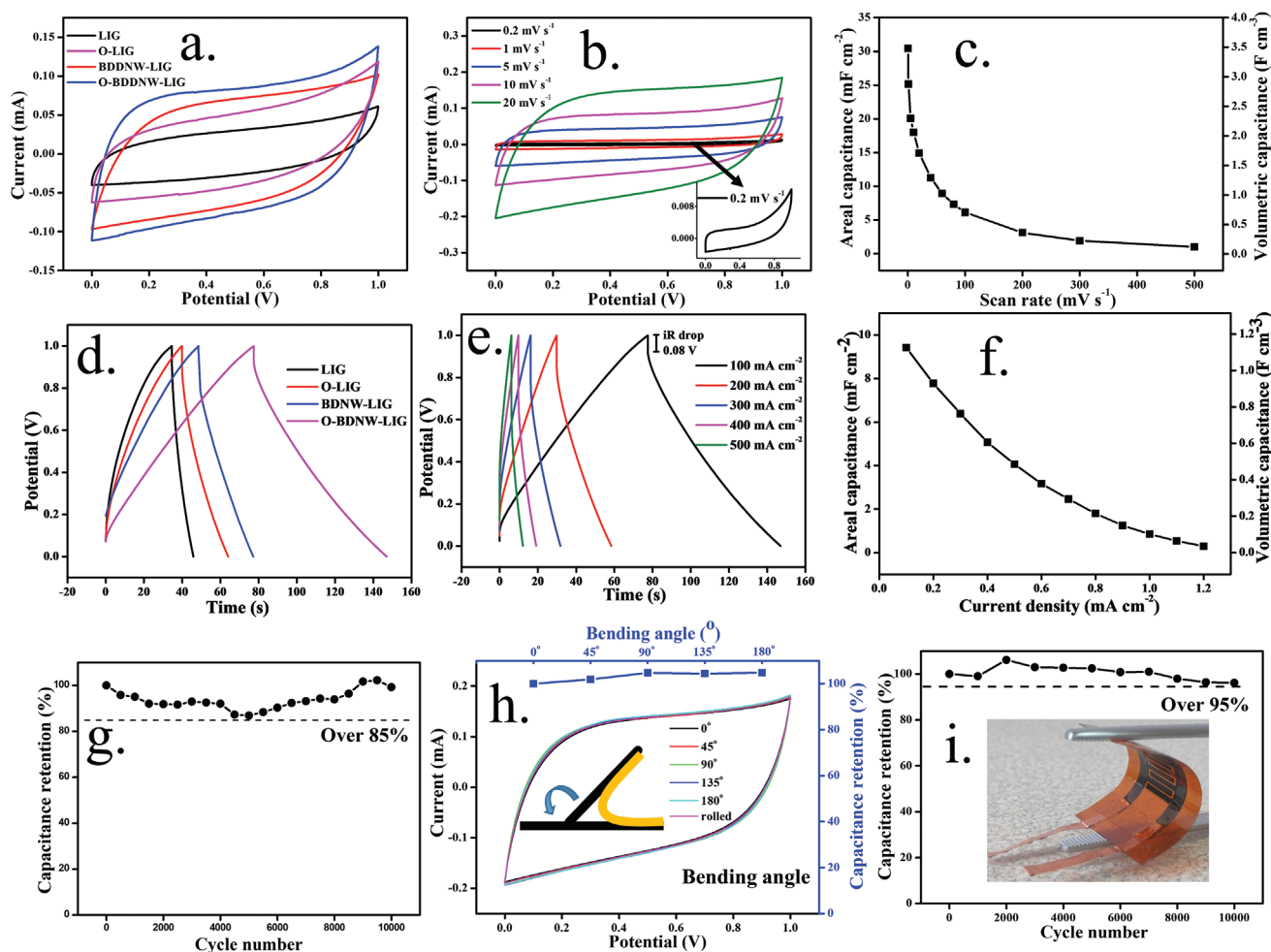
Figure 4. Electrochemical performance of MSCs in PVA-H$_2$SO$_4$ electrolyte. a) Comparison of the CV profiles of LIG, O-LIG, BDNW-LIG, and O-BDNW-LIG at a scan rate of 10 mV s^{-1}. b) CV curves of O-BDNW-LIG at different scan rates. c) Areal and volumetric specific capacitance of O-BDNW-LIG as a function of scan rate. d) Comparison of the GCD curves of LIG, O-LIG, BDNW-LIG, and O-BDNW-LIG at a current density of 0.1 mA cm^{-2}. e) GCD curves of O-BDNW-LIG at a current density range of 0.1–0.5 mA cm^{-2}. f) Areal and volumetric specific capacitance of O-BDNW-LIG calculated from GCD curves as a function of current density. g) Cyclic stability of O-BDNW-LIG over 10 000 charge/discharge cycles. h) CV curves of O-BDNW-LIG under different bending conditions at 20 mV s^{-1}. Mechanical stress does not affect its electrochemical performance. i) Cyclic stability of O-BDNW-LIG under bending conditions. The bent device retains 96% of its initial capacitance after 10 000 charge/discharge cycles. The inset of (I) shows a snapshot of the O-BDNW-LIG MSC device bent with a tweezer.

of O-BDNW-LIG on flexible and wearable electronics, a flexibility test was carried out by CV measurement at 20 mV s^{-1} under different bending conditions (Figure 4h). Regardless of the degree of bending, the MSC device exhibited remarkable EC stability, suggesting good mechanical stability. As can be seen in Figure 4h, the device showed a similar quasi-rectangular CV profile and even larger areas compared to its flat state under different bending conditions, indicating the excellent flexibility of the O-BDNW-LIG MSC. The capacitance was maintained with 100% retention of its initial flat state even when bent over 180°. The MSC device was, therefore, highly flexible and could be bent to extremes without losing its structural integrity. Furthermore, the flexibility endurance test of the device was carried out using GCD measurement by keeping the device bent (Figure 4i). Remarkable cyclic stability was recorded with 96% retention of the initial capacitance after 10 000 cycles. This outstanding EC performance makes O-BDNW-LIG a viable candidate for flexible microelectronics.

Next, depending on the application, capacitors must be linked in series or parallel, similar to batteries, to meet the specific voltage and capacitance rating. The adaptability of the BDNW-LIG MSC device for series and parallel configuration is demonstrated by connecting three devices in both series and parallel combinations (**Figure 5**a–d). As shown in Figure 5a,c, three serially connected O-BDNW-LIG MSCs exhibited a rectangular CV shape and the same discharge time as a single device in the voltage extension of 3 V. Whereas, the current in the CV curves and discharge time of the GCD graphs increased linearly with the number of devices in a parallel combination (Figure 5b–d). Notably, our devices in series combinations could easily power LEDs (red, yellow, and green) (Figure 5f). The ability of the MSC to power LEDs for more than one minute (Movies S2 and S3, Supporting Information) demonstrates their enormous potential for use in powering electronics.

Table 1. Comparison of the specific areal capacitances of laser-induced graphene-based MSCs.

Electrode	$C_{A/CV}$ [mF cm^{-2}]	$C_{A/GCD}$ [mF cm^{-2}]	Refs.
MOF-LIG (MOF-199@ZIF-67)	8.1@1 mV s^{-1} 6.2@10 mV s^{-1}	5.0@0.2 mA cm^{-2}	[66]
LIG prepared from GO films	2.3@10 mV s^{-1}	1.6@0.2 mA cm^{-2}	[1]
LIG prepared from PI films	4.1@1 mV s^{-1}	3.9@0.2 mA cm^{-2}	[8]
LIG prepared from lignin films	15.4@10 mV s^{-1}	12@0.2 mA cm^{-2}	[67]
Laser-induced graphenization of SPEEK film	5.6@3 mV s^{-1}	1.9@0.2 mA cm^{-2}	[68]
TiO$_2$ decorated LIG	–	≈3.3@0.1 mA cm^{-2}	[17]
Boron-doped LIG (5B-LIG)	–	9.54@0.1 mA cm^{-2}	[69]
MXene–rGO composite	34.6		[70]
Laser-induced and KOH-activated 3D grapheme	–	32@0.05 mA cm^{-2}	[71]
Laser-induced nitrogen-self-doped graphite nanofibers	–	57.96@0.02 mA cm^{-2}	[72]
Phosphorus-doped porous LIG	40.4@10 mV s^{-1}	55.5@0.05 mA cm^{-2}	[73]
Boron-doped porous LIG	–	60.6@0.08 mA cm^{-2}	[74]
Nitrogen and boron co-doped LIG	–	40.4@0.05 mA cm^{-2}	[75]
Ruthenium oxide-based LIG	16@20 mV s^{-1}	–	[76]
BDNW decorated oxidized LIG	25.2@1 mV s^{-1} 18@10 mV s^{-1}	9.4@0.1 mA cm^{-2} 7.77@0.2 mA cm^{-2}	Present work

However, the working voltage range of most hydrogel polymer electrolytes rarely exceeds the 1 V window, rendering them unsuitable for many applications. In contrast, ionic liquids (ILs) offer an attractive proposition to the traditional polymer gel/water-based electrolytes due to their broad EC potential window, high ionic conductivity, as well as their superior thermal stability, and nonvolatility.[77] These ILs can be hybridized with some solid components (such as polymers, silica, etc.) to form ionogel, which not only retains the primary characteristics of ILs but also allows easy shaping according to the intended device without leaking issues during flexible operations. Here we mixed EMIMBF$_4$ (48.3 wt%), PAN (12.9 wt%), and TMS (38.8 wt%) to form a clear viscous ionogel. The ionogel integrated into the LIG-based devices and their EC performances are discussed below.
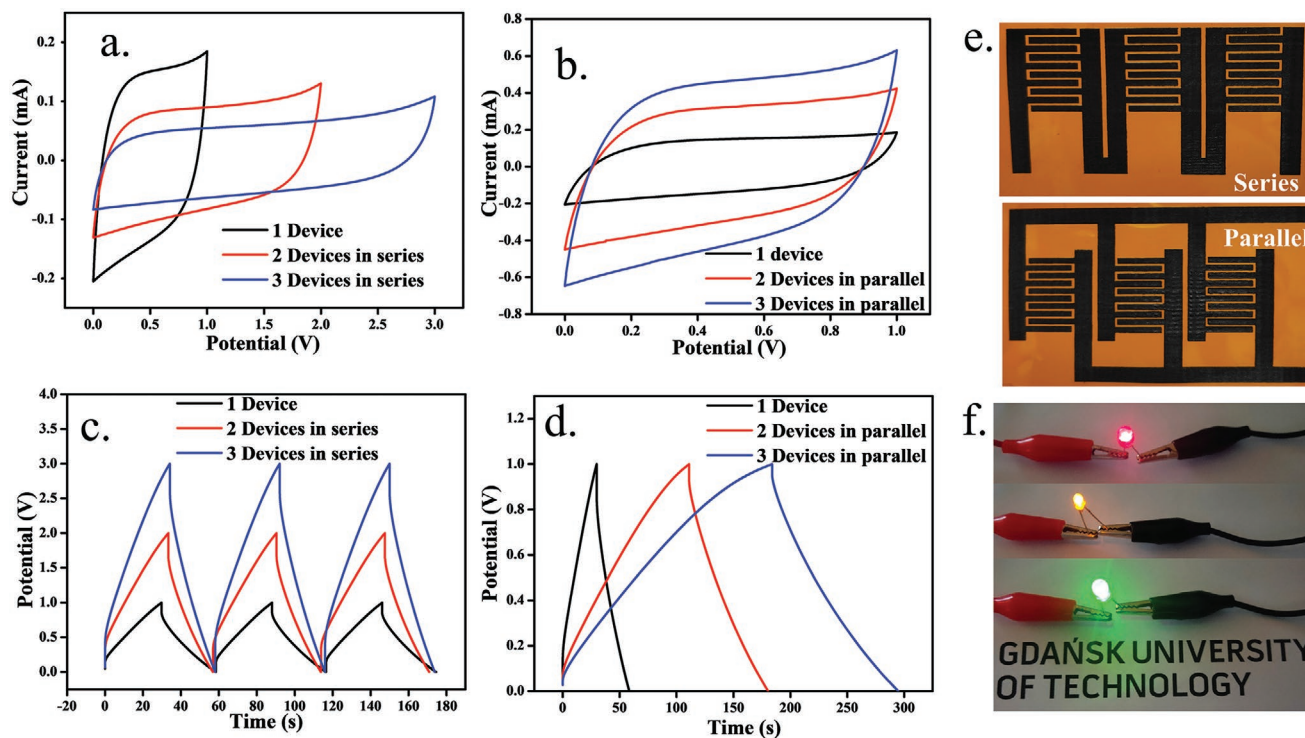
Figure 5. MSC device performance in series/parallel combinations; CV curves at 20 mV s^{-1} and GCD profiles at 0.2 mA cm^{-2} of O-BDNW-LIG MSC devices: a,c) connected in series and b,d) connected in parallel. e) Photographs of the series and parallel connection of the tandem microsupercapacitors. f) Photographs of red, yellow, and green LEDs powered by three serially connected devices.

The EC properties of the LIG, BDNW-LIG, and O-BDNW-LIG were first examined using CV and GCD profiles. Interestingly, as compared to the 1 V working potential in the PVA/H$_2$SO$_4$ electrolyte, all of the devices can now function at a broader potential window of 2 V. As shown in Figure S11 (Supporting Information), the O-BDNW-LIG MSC has a greater areal current density and discharge duration in comparison to the LIG and BDNW-LIG, indicating that oxygen functionalization substantially increased the device capacitance. With the increasing scan rate, the CVs of O-BDNW-LIG showed typical capacitive behavior with a roughly rectangular shape (**Figure 6**a and Figure S12, Supporting Information). The excellent EC properties of the O-BDNW-LIG were also verified by the GCD profile (Figure 6d) with a negligible IR drop. The areal capacitance and volumetric capacitance of the O-BDNW-LIG calculated from the CVs and GCDs are plotted in Figure 6b,e. The O-BDNW-LIG MSC delivered an exceptional areal capacitance of 2.85 mF cm^{-2} and volumetric capacitance of 0.32 F cm^{-3} at 10 mV s^{-1}, both of which are comparable to or even higher than existing LIG-based MSC devices. The MSC device shows excellent cyclic stability as well; with capacitance retention of ≈96% after 10 000 charge/discharge cycles (Figure 6f). To demonstrate the robust flexibility of the O-BDNW-LIG MSC device, we further examined the CV profile under different bending angles ranging from 0 to 180° (Figure 6c). Regardless of the degree of bending, the CV curves had almost similar rectangular shapes and preserved 98% of their initial capacitance even when bent at 180°.

To further demonstrate the scalability and compatibility to high voltage and high capacity powering devices, three serial and parallel O-BDNW-LIG MSC devices were connected without using any metal-based interconnectors or contacts.

As shown in Figure S13 (Supporting Information), the serially connected MSC devices exhibited identical rectangular CV and triangular GCD shapes similar to the single device with a sufficient voltage extension from 2 V for a single cell to 4 and 6 V for two and three tandem cells, respectively. Meanwhile, compared to a single cell, the capacitance was enhanced by linking MSC devices in parallel (Figure S14, Supporting Information). Notably, our devices connected in series can readily power LEDs (Figure S15, Supporting Information), indicating significant potential for real-life powering electronics.

A Ragone plot comparing the areal energy and power densities of the O-BDDNW-LIG with various LIG-based MSC devices is shown in **Figure 7**. When combined with conductive diamond particles and oxygen plasma treatment, the LIG's SC performance improved significantly. For example, the O-BDDNW-LIG exhibited an excellent energy density of ≈1.2 µWh cm^{-2} which is ≈6 times higher than the LIG at 0.2 mA cm^{-2}. Notably, when compared to state-of-the-art ultrahigh-power microsupercapacitors published in the literature, the O-BDDNW-LIG had higher areal energy densities.[8,17,66,68,69,78,79] The excellent energy and power output of our device enables them to compete with commercially available microbatteries and other electrolytic capacitors.

The excellent supercapacitor performance of the O-BDNW-LG in both polymer gel and ionogel electrolyte is attributed to the synergistic combination of the 3D porous network of LIG, outstanding electrochemical stability of BDNW particles, and induced surface defects due to laser irradiation and oxidation process. The combination of the microscale design of the LIG electrode with the fully accessible 3D porous network for the electrolyte is one of the factors for the
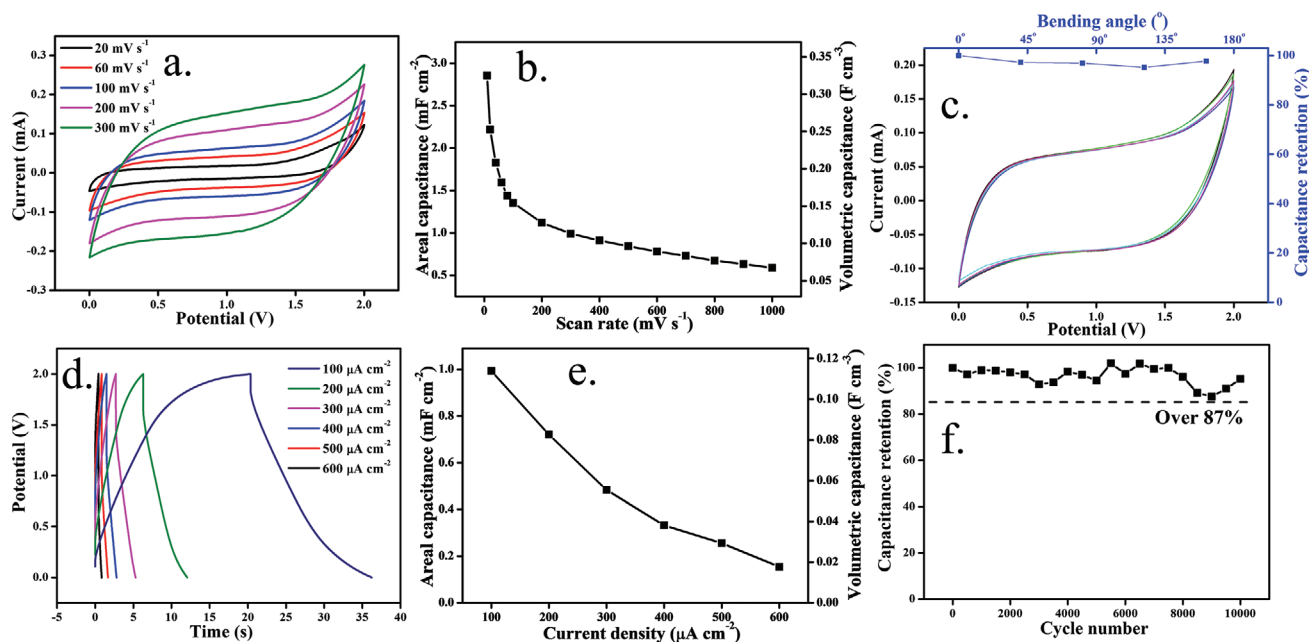
Figure 6. Electrochemical performance of O-BDNW-LIG MSCs in ionogel electrolyte. a) CV curves with varying scan rates. b) Areal and volumetric specific capacitance calculated from CV curves as a function of scan rates. c) CV curves under different bending states at 100 mV s^{-1}. Bending the device has no effect on the electrochemical permanence. d) GCD curves with varying current densities. e) Areal and volumetric specific capacitance calculated from GCD curves as a function of current density. f) Cyclic stability over 10 000 charge–discharge cycles. The device retains ≈96% of its initial capacitance after 10 000 charge–discharge cycles.
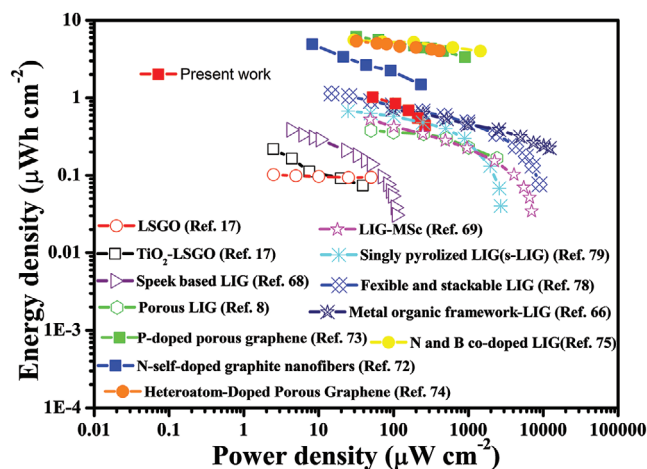
Figure 7. Ragone plot of O-BDNW-LIG MSCs in PVA-H_2SO_4 electrolyte where the areal energy and power density of the MSC device are compared with other state-of-the-art LIG-based energy storage systems.

high-power/energy performance of the LIG-based MSC.[1] The in situ decoration of BDNW on the LIG network improves the MSC device performance even more. The advantage of LIG-BDNW-based MSC device is clearly related to the combination of wide operating potential window, high energy/power density, and device stability even after 10 000 charge/discharge cycles.[27,45,80,81] Here, the BDNW is directly integrated with the LIG network during the photothermal conversion of the PI film, hence the LIG-BDNW hybrid network is structurally stable and not easily collapsed. Efficient charge transport between the BDNW and LIG is achieved through the combination of the sp^2 and sp^3 C−C bonds, i.e., BDNW on LIG exhibits increased conductivity as compared to LIG alone (see Figure S7, Supporting Information).[64,82] Surprisingly, the MSC device performance is improved significantly for the O-BDNW-LIG when compared with LIG and BDNW-LIG. The introduction of oxygen-containing groups favorably introduces additional capacitance of the LIG-BDNW hybrid by improving its hydrophilicity. The enhanced hydrophilicity of the O-BDNW-LIG provides better contact with the PVA/H_2SO_4 electrolyte.[83] The wettability of the active electrode material in the electrolyte is crucial to improving the MSC device performance, where better electrolyte contact at the electrode surface leads to efficient capillary action of the micropores, thus improving the ion-accessible surface area.[84,85] In addition, the increased degree of defect and active sites (as observed in the Raman spectra) due to O_2 plasma treatment also partially improves the charge storage capacity of the O-BDNW-LIG, as is described theoretically and experimentally.[8,84] Therefore, by combining the dual advantage of sp^2 (LIG) and sp^3 (BDNW) and by incorporating oxygenated surface functionalities within the sp^2–sp^3 hybrid network, the MSC device performance can be significantly enhanced.

3. Conclusion

We have developed and demonstrated a straightforward strategy to fabricate solid-state flexible MSC devices with in-plane interdigitated electrodes using the combination of sp^2 (LIG) and sp^3 (BDNW) diamond/nanowall in a hybrid composite material. The room temperature and ambient air-based laser scribing on BDNW-coated PI film is followed by O_2 plasma treatment to induce the surface defects and control its wettability. Moreover, laser-induced thermal shock can drastically reduce the thermal resistance of the diamond particles, which can trigger the current carrying capacity of LIG. At an elevated temperate, we can improve the LIG current carrying capacity thermally. The solid-state symmetric flexible O-BDNW-LIG MSCs demonstrate high specific capacitance (7.77 mF cm^{-2} at a current density of 0.2 mA cm^{-2}), excellent energy/power output, good cyclic performance (98% capacitance retention after 10 000 charge/discharge cycles), and mechanical flexibilities. Without using any organic binders, additional current collectors, or conductive additives, which are often required for any commercial microelectronics, the present work allows for the fabrication of MSC devices with improved energy storage performance due to the ease with which ions can access the active material. Therefore, in a time of high demand for smart materials with high energy storage capacity, the present work not only demonstrates the applicability of the LIG technique in the presence of diamond, but the findings are also important for the application of LIG to high-frequency transistors, interconnects, etc., which can lead to new carbon on carbon (sp^3 on sp^2) technology.

Supporting Information

Supporting Information is available from the Wiley Online Library or from the author.

Conflict of Interest

The authors declare no conflict of interest.

Data Availability Statement

The data that support the findings of this study are available from the corresponding author upon reasonable request.

**ADVANCED
SCIENCE NEWS**

www.advancedsciencenews.com

**ADVANCED
FUNCTIONAL
MATERIALS**

www.afm-journal.de

[1] M. F. El-Kady, R. B. Kaner, *Nat. Commun.* **2013**, *4*, 1475.

[2] J. W. Lee, R. Xu, S. Lee, K.-I. Jang, Y. Yang, A. Banks, K. J. Yu, J. Kim, S. Xu, S. Ma, S. W. Jang, P. Won, Y. Li, B. H. Kim, J. Y. Choe, S. Huh, Y. H. Kwon, Y. Huang, U. Paik, J. A. Rogers, *Proc. Natl. Acad. Sci. USA* **2016**, *113*, 6131LP.

[3] W. Song, B. Gan, T. Jiang, Y. Zhang, A. Yu, H. Yuan, N. Chen, C. Sun, Z. L. Wang, *ACS Nano* **2016**, *10*, 8097.

[4] S. Jung, J. Lee, T. Hyeon, M. Lee, D.-H. Kim, *Adv. Mater.* **2014**, *26*, 6329.

[5] P. Huang, C. Lethien, S. Pinaud, K. Brousse, R. Laloo, V. Turq, M. Respaud, A. Demortière, B. Daffos, P. L. Taberna, B. Chaudret, Y. Gogotsi, P. Simon, *Science* **2016**, *351*, 691.

[6] M. F. El-Kady, V. Strong, S. Dubin, R. B. Kaner, *Science* **2012**, *335*, 1326.

[7] R. Ye, D. K. James, J. M. Tour, *Adv. Mater.* **2019**, *31*, 1803621.

[8] J. Lin, Z. Peng, Y. Liu, F. Ruiz-Zepeda, R. Ye, E. L. G. Samuel, M. J. Yacaman, B. I. Yakobson, J. M. Tour, *Nat. Commun.* **2014**, *5*, 5714.

[9] B. Hsia, J. Marschewski, S. Wang, J. Bin In, C. Carraro, D. Poulikakos, C. P. Grigoropoulos, R. Maboudian, *Nanotechnology* **2014**, *25*, 055401.

[10] J. Lin, C. Zhang, Z. Yan, Y. Zhu, Z. Peng, R. H. Hauge, D. Natelson, J. M. Tour, *Nano Lett.* **2013**, *13*, 72.

[11] P. Huang, M. Heon, D. Pech, M. Brunet, P.-L. Taberna, Y. Gogotsi, S. Lofland, J. D. Hettinger, P. Simon, *J. Power Sources* **2013**, *225*, 240.

[12] C. John, L. Celine, T. Pierre-Louis, S. Patrice, G. Yury, *Science* **2010**, *328*, 480.

[13] X. Wang, Y. Yin, X. Li, Z. You, *J. Power Sources* **2014**, *252*, 64.

[14] X. Wang, B. D. Myers, J. Yan, G. Shekhawat, V. David, P. S. Lee, *Nanoscale* **2013**, *5*, 4119.

[15] C. Shen, X. Wang, S. Li, J. Wang, W. Zhang, F. Kang, *J. Power Sources* **2013**, *234*, 302.

[16] Z.-S. Wu, K. Parvez, S. Li, S. Yang, Z. Liu, S. Liu, X. Feng, K. Müllen, *Adv. Mater.* **2015**, *27*, 4054.

[17] L. Fornasini, S. Scaravonati, G. Magnani, A. Morenghi, M. Sidoli, D. Bersani, G. Bertoni, L. Aversa, R. Verucchi, M. Riccò, P. P. Lottici, D. Pontiroli, *Carbon* **2021**, *176*, 296.

[18] A. Huang, M. F. El-Kady, X. Chang, M. Anderson, C.-W. Lin, C. L. Turner, R. B. Kaner, *Adv. Energy Mater.* **2021**, *11*, 2100768.

[19] P. Simon, Y. Gogotsi, *Acc. Chem. Res.* **2013**, *46*, 1094.

[20] N. Yang, S. Yu, J. V Macpherson, Y. Einaga, H. Zhao, G. Zhao, G. M. Swain, X. Jiang, *Chem. Soc. Rev.* **2019**, *48*, 157.

[21] C. Hébert, J. P. Mazellier, E. Scorsone, M. Mermoux, P. Bergonzo, *Carbon* **2014**, *71*, 27.

[22] C. Hébert, E. Scorsone, M. Mermoux, P. Bergonzo, *Carbon* **2015**, *90*, 102.

[23] F. Gao, C. E. Nebel, *ACS Appl. Mater. Interfaces* **2016**, *8*, 28244.

[24] G. M. Swain, A. B. Anderson, J. C. Angus, *MRS Bull.* **1998**, *23*, 56.

[25] R. Hoffmann, A. Kriele, H. Obloh, J. Hees, M. Wolfer, W. Smirnov, N. Yang, C. E. Nebel, *Appl. Phys. Lett.* **2010**, *97*, 052103.

[26] H. B. Martin, *J. Electrochem. Soc.* **1996**, *143*, L133.

[27] N. Yang, J. S. Foord, X. Jiang, *Carbon* **2016**, *99*, 90.

[28] R. Hoffmann, H. Obloh, N. Tokuda, N. Yang, C. E. Nebel, *Langmuir* **2012**, *28*, 47.

[29] Z. Jian, N. Yang, M. Vogel, S. Leith, A. Schulte, H. Schönherr, T. Jiao, W. Zhang, J. Müller, B. Butz, X. Jiang, *Adv. Energy Mater.* **2020**, *10*, 2002202.

[30] J. Xu, N. Yang, S. Heuser, S. Yu, A. Schulte, H. Schönherr, X. Jiang, *Adv. Energy Mater.* **2019**, *9*, 1803623.

[31] W. Wu, L. Yang, S. Chen, Y. Shao, L. Jing, G. Zhao, H. Wei, *RSC Adv.* **2015**, *5*, 91645.

[32] D. M. Jang, H. S. Im, S. H. Back, K. Park, Y. R. Lim, C. S. Jung, J. Park, M. Lee, *Phys. Chem. Chem. Phys.* **2014**, *16*, 2411.

[33] J. Xiao, G. Ouyang, P. Liu, C. X. Wang, G. W. Yang, *Nano Lett.* **2014**, *14*, 3645.

[34] D. X. Luong, K. Yang, J. Yoon, S. P. Singh, T. Wang, C. J. Arnusch, J. M. Tour, *ACS Nano* **2019**, *13*, 2579.

[35] S. Deshmukh, D. Banerjee, J. S. M. Quintero, S. J. Fishlock, J. McLaughlin, P. R. Waghmare, S. S. Roy, *Carbon* **2021**, *182*, 605.

[36] H. Liu, Y. Tang, Y. Xie, L. Lu, Z. Wan, W. Tang, L. Yang, D. Yang, *Surf. Coat. Technol.* **2019**, *361*, 102.

[37] A. Tiliakos, C. Ceaus, S. M. Iordache, E. Vasile, I. Stamatin, *J. Anal. Appl. Pyrol.* **2016**, *121*, 275.

[38] J. Zhang, M. Ren, L. Wang, Y. Li, B. I. Yakobson, J. M. Tour, *Adv. Mater.* **2018**, *30*, 1707319.

[39] R. Chetty, K. K. Maniam, W. Schuhmann, M. Muhler, *ChemPlusChem* **2015**, *80*, 130.

[40] X. Yan, J. Wei, K. An, Y. Zhao, J. Liu, L. Chen, L. Hei, C. Li, *Diamond Relat. Mater.* **2018**, *87*, 267.

[41] Y. Rho, H. Kang, C. P. Grigoropoulos, K.-T. Kang, *Appl. Phys. A* **2020**, *126*, 703.

[42] S. Deshmukh, K. J. Sankaran, D. Banerjee, C. J. Yeh, K. C. Leou, D. M. Phase, M. Gupta, I. N. Lin, K. Haenen, S. S. Roy, P. R. Waghmare, *J. Mater. Chem. A* **2019**, *7*, 19026.

[43] S. Deshmukh, D. Banerjee, G. Bhattacharya, S. J. Fishlock, A. Barman, J. McLaughlin, S. S. Roy, *ACS Appl. Nano Mater.* **2020**, *3*, 4084.

[44] P. W. May, W. J. Ludlow, M. Hannaway, P. J. Heard, J. A. Smith, K. N. Rosser, *Diamond Relat. Mater.* **2008**, *17*, 105.

[45] D. Banerjee, K. J. Sankaran, S. Deshmukh, M. Ficek, G. Bhattacharya, J. Ryl, D. M. Phase, M. Gupta, R. Bogdanowicz, I. N. Lin, A. Kanjilal, K. Haenen, S. S. Roy, *J. Phys. Chem. C* **2019**, *123*, 15458.

[46] N. Spătaru, J. M. Calderon-Moreno, P. Osiceanu, T. Kondo, C. Terashima, M. Popa, M. M. Radu, D. Culiță, L. Preda, M. A. Mihai, T. Spătaru, *Chem. Eng. J.* **2020**, *402*, 126258.

[47] L. G. Cançado, M. A. Pimenta, R. Saito, A. Jorio, L. O. Ladeira, A. Grueneis, A. G. Souza-Filho, G. Dresselhaus, M. S. Dresselhaus, *Phys. Rev. B* **2002**, *66*, 35415.

[48] Y. Wang, M. Jaiswal, M. Lin, S. Saha, B. Özyilmaz, K. P. Loh, *ACS Nano* **2012**, *6*, 1018.

[49] P. Venezuela, M. Lazzeri, F. Mauri, *Phys. Rev. B* **2011**, *84*, 35433.

[50] A. Eckmann, A. Felten, A. Mishchenko, L. Britnell, R. Krupke, K. S. Novoselov, C. Casiraghi, *Nano Lett.* **2012**, *12*, 3925.

[51] K. Krishnamoorthy, M. Veerapandian, K. Yun, S.-J. Kim, *Carbon* **2013**, *53*, 38.

[52] S. T. Lee, H. Y. Peng, X. T. Zhou, N. Wang, C. S. Lee, I. Bello, Y. Lifshitz, *Science* **2000**, *287*, 104.

[53] P.-G. Ren, D.-X. Yan, X. Ji, T. Chen, Z.-M. Li, *Nanotechnology* **2010**, *22*, 055705.

[54] M. Pierpaoli, M. Ficek, P. Jakóbczyk, J. Karczewski, R. Bogdanowicz, *Acta Mater.* **2021**, *214*, 116989.

[55] M. Ficek, B. Dec, K. J. Sankaran, K. Gajewski, P. Tatarczak, I. Wlasny, A. Wysmolek, K. Haenen, T. Gotszalk, R. Bogdanowicz, *Adv. Mater. Interfaces* **2021**, *8*, 2100464.

[56] L. Torrisi, L. Silipigni, M. Cutroneo, A. Torrisi, *Vacuum* **2020**, *173*, 109175.

[57] H. Ma, C. Li, M. Zhang, J.-D. Hong, G. Shi, *J. Mater. Chem. A* **2017**, *5*, 17040.

[58] Z. Li, Z. Xu, H. Wang, J. Ding, B. Zahiri, C. M. B. Holt, X. Tan, D. Mitlin, *Energy Environ. Sci.* **2014**, *7*, 1708.

[59] H. Ma, Q. Zhou, M. Wu, M. Zhang, B. Yao, T. Gao, H. Wang, C. Li, D. Sui, Y. Chen, G. Shi, *J. Mater. Chem. A* **2018**, *6*, 6587.

[60] T. Takai, T. Halicioğlu, W. A. Tiller, *Surf. Sci.* **1985**, *164*, 341.

[61] S. K. Rhee, *J. Am. Ceram. Soc.* **1972**, *55*, 300.

[62] M. Sobaszek, K. Siuzdak, J. Ryl, M. Sawczak, S. Gupta, S. B. Carrizosa, M. Ficek, B. Dec, K. Darowicki, R. Bogdanowicz, *J. Phys. Chem. C* **2017**, *121*, 20821.

[63] E. Koudoumas, O. Kokkinaki, M. Konstantaki, S. Couris, S. Korovin, P. Detkov, V. Kuznetsov, S. Pimenov, V. Pustovoi, *Chem. Phys. Lett.* **2002**, *357*, 336.

[64] J. Yu, G. Liu, A. V Sumant, V. Goyal, A. A. Balandin, *Nano Lett.* **2012**, *12*, 1603.

2206097 (11 of 12)

**ADVANCED
SCIENCE NEWS**

www.advancedsciencenews.com

**ADVANCED
FUNCTIONAL
MATERIALS**

www.afm-journal.de

[65] H. Xiao, Z.-S. Wu, L. Chen, F. Zhou, S. Zheng, W. Ren, H.-M. Cheng, X. Bao, *ACS Nano* **2017**, *11*, 7284.

[66] W. Zhang, R. Li, H. Zheng, J. Bao, Y. Tang, K. Zhou, *Adv. Funct. Mater.* **2021**, *31*, 2009057.

[67] W. Zhang, Y. Lei, F. Ming, Q. Jiang, P. M. F. J. Costa, H. N. Alshareef, *Adv. Energy Mater.* **2018**, *8*, 1801840.

[68] A. Lamberti, M. Serrapede, G. Ferraro, M. Fontana, F. Perrucci, S. Bianco, A. Chiolerio, S. Bocchini, *2D Mater.* **2017**, *4*, 035012.

[69] Z. Peng, R. Ye, J. A. Mann, D. Zakhidov, Y. Li, P. R. Smalley, J. Lin, J. M. Tour, *ACS Nano* **2015**, *9*, 5868.

[70] Y. Yue, N. Liu, Y. Ma, S. Wang, W. Liu, C. Luo, H. Zhang, F. Cheng, J. Rao, X. Hu, J. Su, Y. Gao, *ACS Nano* **2018**, *12*, 4224.

[71] H. Liu, Y. Xie, J. Liu, K. Moon, L. Lu, Z. Lin, W. Yuan, C. Shen, X. Zang, L. Lin, Y. Tang, C.-P. Wong, *Chem. Eng. J.* **2020**, *393*, 124672.

[72] H. Liu, Y. Xie, J. Li, Z. Sun, J. Liu, K. Moon, L. Lu, Y. Chen, Y. Tang, X. Chen, C.-P. Wong, *Chem. Eng. J.* **2021**, *404*, 126375.

[73] Y. Rao, M. Yuan, F. Luo, Z. Wang, H. Li, J. Yu, X. Chen, *Carbon* **2021**, *180*, 56.

[74] M. Yuan, F. Luo, Z. Wang, H. Li, Y. Rao, J. Yu, Y. Wang, D. Xie, X. Chen, C.-P. Wong, *ACS Appl. Mater. Interfaces* **2021**, *13*, 22426.

[75] M. Khandelwal, C. Van Tran, J. Lee, J. Bin In, *Chem. Eng. J.* **2022**, *428*, 131119.

[76] K. Brousse, S. Pinaud, S. Nguyen, P.-F. Fazzini, R. Makarem, C. Josse, Y. Thimont, B. Chaudret, P.-L. Taberna, M. Respaud, P. Simon, *Adv. Energy Mater.* **2020**, *10*, 1903136.

[77] J. F. Wishart, *Energy Environ. Sci.* **2009**, *2*, 956.

[78] Z. Peng, J. Lin, R. Ye, E. L. G. Samuel, J. M. Tour, *ACS Appl. Mater. Interfaces* **2015**, *7*, 3414.

[79] K. Y. Kim, H. Choi, C. Van Tran, J. Bin In, *J. Power Sources* **2019**, *441*, 227199.

[80] D. Banerjee, K. J. Sankaran, S. Deshmukh, M. Ficek, C.-J. Yeh, J. Ryl, I.-N. Lin, R. Bogdanowicz, A. Kanjilal, K. Haenen, *Nanoscale* **2020**, *12*, 10117.

[81] D. Cui, H. Li, M. Li, C. Li, L. Qian, B. Zhou, B. Yang, *ACS Appl. Energy Mater.* **2019**, *2*, 1526.

[82] F. Zhao, A. Vrajitoarea, Q. Jiang, X. Han, A. Chaudhary, J. O. Welch, R. B. Jackman, *Sci. Rep.* **2015**, *5*, 13771.

[83] L. Li, Q. Zhong, N. D. Kim, G. Ruan, Y. Yang, C. Gao, H. Fei, Y. Li, Y. Ji, J. M. Tour, *Carbon* **2016**, *105*, 260.

[84] Y. Li, D. X. Luong, J. Zhang, Y. R. Tarkunde, C. Kittrell, F. Sargunaraj, Y. Ji, C. J. Arnusch, J. M. Tour, *Adv. Mater.* **2017**, *29*, 1700496.

[85] Z. Li, S. Gadipelli, Y. Yang, G. He, J. Guo, J. Li, Y. Lu, C. A. Howard, D. J. L. Brett, I. P. Parkin, F. Li, Z. Guo, *Energy Storage Mater.* **2019**, *17*, 12.